IEEE Open Journal of Antennas and Propagation

Received XX Month, XXXX; revised XX Month, XXXX; accepted XX Month, XXXX; Date of publication XX Month, XXXX; date of current version XX Month, XXXX.

Digital Object Identifier 10.1109/OJAP.2020.1234567

Hybrid Integration of a Beam-Steering Leaky-Wave Antenna and Power Amplifier MMIC using UPD Printing in 220 to 325 GHz Range

Georg Gramlich*, Elizabeth Bekker*, Luca Valenziano*, Joel Dittmer*, Martin Roemhild†, Holger Baur†, Fabian Thome‡, Axel Tessmann‡, Michael Kuri‡, Tom Neerfeld§, Andreas Stöhr§, Sebastian Randel*, Christian Koos*, Norbert Fruehauf†, Thomas Zwick*, Akanksha Bhutani*

[1]Karlsruhe Institute of Technology (KIT), Germany
[2]University of Stuttgart, Germany
[3]Fraunhofer Institute for Applied Solid State Physics IAF, Germany
[4]University of Duisburg Essen (UDE), Germany

CORRESPONDING AUTHOR: Georg Gramlich (e-mail: georg.gramlich@kit.edu).

This research is supported by the Ministry of Science, Research, and the Arts of the state of Baden-Wuerttemberg, Germany, within the framework of the "Mobility of the Future" Innovation Campus (ICM).
This work is financially supported by the Federal Ministry of Education and Research of Germany in the project "Open6GHub" (grant number: 16KISK010).
This work is supported in part by Finetech GmbH & Co.KG.

ABSTRACT

This paper presents the first hybrid-integration assembly of a power amplifier (PA) monolithic microwave integrated circuit (MMIC) and a beam-steering leaky wave antenna (LWA) using an ultra-precise deposition (UPD) printed coplanar waveguide (CPW) interconnect operating in a broad sub-THz range of $220\,\mathrm{GHz}$ to $325\,\mathrm{GHz}$. The hybrid assembly uses an InGaAs PA with a saturated output power of up to $14.5\,\mathrm{dBm}$ and an InP LWA with a peak antenna gain of up to $13.5\,\mathrm{dBi}$ and a beam-steering range from $-60°$ to $35°$. The hybrid assembly employs a submount that compensates for the height difference of $\approx 300\,\mu\mathrm{m}$ between the PA MMIC and LWA substrates. The PA MMIC and LWA are positioned at an edge-to-edge distance of just $11\,\mu\mathrm{m}$ on the submount using a die bonder with sub-micrometer accuracy. The small gap between the PA MMIC and LWA is filled with a polymer that provides a stable dielectric constant in the target sub-THz range. The UPD-printed CPW interconnect is optimized to maintain a characteristic impedance of $50\,\Omega$ by analyzing the dielectric properties and thickness of the various materials on which the printing is performed. Moreover, the surface topology is measured using a white light interferometer, to enable fully conformal printing. The electromagnetic simulation results of the CPW interconnect show an insertion loss of $1.1\,\mathrm{dB}$ to $1.7\,\mathrm{dB}$, which includes the RF pads of the PA MMIC, LWA, and the short segments of CPW designed on the PA MMIC and LWA substrates. A separate UPD-printed CPW test assembly is manufactured on a single polymer substrate, and custom through-reflect-line calibration standards are printed on the same substrate to experimentally validate the insertion loss of a UPD-printed CPW in the $220\,\mathrm{GHz}$ to $325\,\mathrm{GHz}$ range. A probe-based measurement setup is used to characterize the hybrid assembly. The hybrid assembly achieves a reflection coefficient of less than $-10\,\mathrm{dB}$ and a peak gain of up to $26\,\mathrm{dBi}$ across the sub-THz range. The beam-steering functionality of the hybrid assembly is successfully validated only in the forward quadrant due to measurement restrictions in the backward quadrant. In the forward quadrant, the measured beam-steering angle of the hybrid assembly varies from $0°$ to $37°$, which is in good agreement with the standalone LWA.

INDEX TERMS beam-steering, leaky-wave, MMIC, power amplifier, UPD printing, sub-THz antenna.

I. INTRODUCTION

The sub-THz frequency range is currently being explored for sixth-generation (6G) wireless communication [1], [2]. The large absolute bandwidth in the sub-THz range promises ultra-high data rates of up to hundreds of gigabits per second. Therefore, it is envisioned as a key enabler for applications such as holographic connectivity, device-to-device communication, hotspot downloading, and wireless cellular fronthaul/backhaul networks [3]. Furthermore, the first IEEE standard for wireless communication, IEEE Std. 802.15.3d, is established in the sub-THz range from $252\,\mathrm{GHz}$ to $325\,\mathrm{GHz}$ [4]. One of the main challenges of deploying a sub-THz wireless link in a line-of-sight scenario is the extremely high free-space path loss (FSPL), which increases quadratically with frequency and distance. Under normal weather conditions, the FSPL dominates over atmospheric loss, provided the wireless link operates within the so-called atmospheric window. One of these atmospheric windows exists from $220\,\mathrm{GHz}$ to $325\,\mathrm{GHz}$ [5]. To overcome propagation loss and make a sub-THz wireless link feasible over a distance of several meters, a transmitter (Tx) radio frequency (RF) frontend operating in the sub-THz range with a high effective isotropic radiated power (EIRP) is required [6]. Such a Tx RF frontend requires integration of a sub-THz power amplifier (PA) with high saturated output power and a sub-THz high-gain antenna.

Furthermore, in accordance with the requirements of future 6G wireless systems, a Tx RF frontend should provide beam-steering functionality, which can serve multiple users simultaneously with high data rates in a sub-THz point-to-multipoint wireless link [3]. Beam-steering frontends implemented at frequencies up to the millimeter-wave range typically use phase shifters to steer the beam of an antenna array in the desired direction (i.e., phased array) [7], [8]. However, a passive phase shifter results in a high insertion loss of up to $15.6\,\mathrm{dB}$ in $220\,\mathrm{GHz}$ to $320\,\mathrm{GHz}$ range [9]. Moreover, in a phased array, the complexity of feed control increases with the required angular resolution, and a phased array Tx typically serves single user at a time. Digital beamforming, on the other hand, can serve multiple users with parallel data streams. However, it faces challenges related to high circuit complexity and power consumption, which become even more pronounced in the sub-THz range [10]. Alternatively, a leaky-wave antenna (LWA) provides a simple means of achieving one-dimensional beam-steering in the sub-THz range. The beam steers in the spatial domain as the frequency sweeps over the antenna's operational bandwidth [10], [11]. Unlike a phased array, high angular resolution can be easily achieved with a high-gain sub-THz LWA. Furthermore, the feed control of an LWA beam-steering frontend is much simpler, and it can serve multiple users simultaneously with pencil beams pointing in different spatial directions. Compared to digital beamforming, an LWA beam-steering frontend saves power consumption, as it does not require numerous power-hungry analog-to-digital converters. Additionally, the digital signal processing required for the latter is much simpler. An LWA provides a simple means of achieving beam-steering in the sub-THz range, compared to beam-steering frontends based on phased array and digital beamforming. The only limitation of an LWA beam-steering frontend is that the signal bandwidth available per user is constrained by the LWA beamwidth [12]. This is not the case with phased array or digital beamforming, where the full antenna bandwidth can be used to transmit signal in a specific spatial direction.

In an LWA, the electromagnetic wave gradually leaks over an antenna aperture that is several wavelengths long to produce the desired radiation characteristics [13]. Implementing such an antenna on-chip is extremely cost-intensive, since the on-chip area available for realizing the antenna is very limited, typically on the order of $1\,\mathrm{mm}\times0.75\,\mathrm{mm}$ [14]. Therefore, hybrid integration of an LWA and a PA operating in the sub-THz range is necessary. Although some LWAs have been demonstrated in the sub-THz range to date [15]–[20], the hybrid integration of an LWA with a PA monolithic microwave integrated circuit (MMIC), resulting in a miniaturized hybrid assembly, has not been achieved. This is shown for the first time in this work to the best of the authors' knowledge. The miniaturized hybrid assembly thus paves the way for realizing a beam-steering Tx RF frontend that can be employed in a multi-user sub-THz link operating over a distance of several meters with a high data rate in future 6G wireless systems.

The goal of this work is to achieve the hybrid integration of a PA MMIC and an LWA over a broad sub-THz range from $220\,\mathrm{GHz}$ to $325\,\mathrm{GHz}$. The PA MMIC used in this work is based on $35\,\mathrm{nm}$ InGaAs mHEMT technology, providing a high saturated output power of up to $14.5\,\mathrm{dBm}$ in the target sub-THz range [21]. The LWA used here is based on an InP process, with a peak antenna gain of up to $13.5\,\mathrm{dBi}$ and a beam-steering range of -60° to 35° in the target sub-THz range [16]. The PA MMIC-to-LWA interconnect should have low insertion loss and good impedance matching across the target sub-THz range. In [22], a single wirebond of length $100\,\mu\mathrm{m}$ connects a $280\,\mathrm{GHz}$ to $310\,\mathrm{GHz}$ GaAs frequency multiplier MMIC and a quartz stacked patch antenna. The simulated S-parameters of the wirebond interconnect show an insertion loss of 3 to $4\,\mathrm{dB}$. In [23], a differential wirebond connects a $246\,\mathrm{GHz}$ SiGe BiCMOS BPSK Tx chip to a PCB antenna. The differential wirebond interconnect has an insertion loss of less than $6\,\mathrm{dB}$ [24]. In [25], an air-bridge differential interconnect based on spray coating and laser lithography connects a $220\,\mathrm{GHz}$ to $320\,\mathrm{GHz}$ GaAs balun to a quartz-cavity LW feed. The differential interconnect has a low loss of $0.2\,\mathrm{dB}$, whereas the assembly loss, including the interconnect, balun, and $730\,\mu\mathrm{m}$ long feed line on quartz, varies between $2.1\,\mathrm{dB}$ and $2.7\,\mathrm{dB}$. Furthermore, in [26], a $250\,\mu\mathrm{m}$ long coplanar waveguide (CPW) interconnect based on a redistribution layer is flipped on InP and Si MMICs

This work is licensed under a Creative Commons Attribution 4.0 License. For more information, see https://creativecommons.org/licenses/by/4.0/

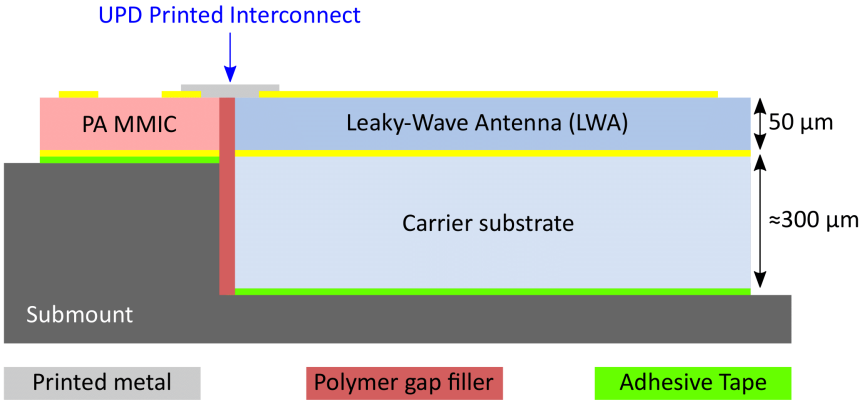

FIGURE 1: Schematic of a hybrid-integration assembly consisting of a PA MMIC and an LWA connected by UPD printing.

using 3 µm height contact vias. The CPW interconnect shows an insertion loss of less than 4 dB at 300 GHz.

In recent years, there has been a significant increase in research on printed RF interconnects, as printing offers greater flexibility compared to conventional interconnect technologies such eWLB bonding and flip-chip. At the same time, printed interconnects eliminate the inherent parasitic effects associated with wire bonding and flip-chip. Among printing techniques, most of the research conducted to date has focused on Aerosol Jet (AJ) printing. However, work on integrating MMICs with AJ printed interconnects in the sub-THz range has been limited to a maximum operating frequency of 210 GHz [27], [28]. Another printing technique, based on direct-write multi-photon laser lithography has been used to demonstrate a 274 GHz elevated slot antenna and a printed CPW operating up to 330 GHz. However, hybrid integration with an MMIC was not achieved in this work [29]. The printing technique used in this work is based on Ultra-Precise Deposition (UPD). UPD is a highly promising technique for producing high-precision, low-cost passive components [30]–[32]. UPD comes with the invaluable advantage of being able to create minimum feature and gap sizes down to 1 µm [33], compared to 10 µm for AJ printing [34] and 20 µm for inkjet printing [35]. As operating frequencies increase, the required RF structures become smaller. Therefore, UPD has a decisive advantage over the other two printing technologies in the sub-THz range of 220 GHz to 325 GHz, which is the operating range of the hybrid-integration assembly shown in this work. Additionally, AJ printing suffers from overspray, which can cause short circuits when small gap sizes are required, severely diminishing yield. Inkjet printing, on the other hand, has the downside of strong substrate-ink interaction, which becomes very challenging when printing over a multitude of different substrates, as in this application, since the contact angle and, therefore, droplet size change from substrate to substrate. UPD, however, has very low ink-to-substrate interaction due to the high viscosity of the printed ink and does not exhibit any overspray, as it is a direct-write technology. It is, therefore, the only technology capable of reliably achieving the required structure sizes necessary in this application to maintain a constant 50 Ω characteristic impedance over the entire length of the interconnect. UPD has previously been used to realize planar and dielectric ramp-based RF interconnects operating up to a maximum frequency of 170 GHz [30], [36]. However, UPD applications demonstrated to date have focused on the lower sub-THz range, with a maximum frequency of up to 170 GHz. Furthermore, these applications have not demonstrated hybrid integration with an active MMIC.

To summarize, the paper presents the first hybrid-integration assembly of a PA MMIC and an LWA using the UPD printing technique, operating over a broad sub-THz range of 220 GHz to 325 GHz. To the best of the authors' knowledge, this work is the first to use a printed interconnect to connect an active MMIC and an antenna, achieving the highest operating frequency, the highest peak gain, and the lowest insertion loss for a sub-THz hybrid assembly demonstrated to date. This work paves the way for a beam-steering Tx RF frontend that can be used in a sub-THz multi-user link operating over a distance of several meters with a high data rate in future 6G wireless systems. The paper is organized as follows: Section II provides an overview of the hybrid assembly, followed by a description of its components, including the PA MMIC, LWA, and the UPD printed interconnect. It presents the simulation results of the hybrid assembly and compares them to those of the LWA. Section III describes the manufacturing process, detailing all relevant steps, materials, and equipment involved in the hybrid-integration assembly. Section IV presents the experimental validation of a UPD-printed CPW test assembly using probe-based two-port S-parameter measurements. It also describes the probe-based measurement setup used to characterize the hybrid-integration assembly, followed by the measurement results and their analysis. Section V concludes the paper and presents an outlook for this work.

II. Assembly Overview and System Simulation

The concept of a hybrid-integration assembly of a PA MMIC and LWA based on a UPD-printed interconnect is shown in

Fig. 1. A 300 µm thick carrier substrate provides mechanical stability to the InP LWA, and a metal submount with precisely milled steps ensures that the top metal layers of the PA MMIC and the LWA are at the same height. The UPD printing process is used to connect the PA MMIC and the LWA. The PA MMIC is based on a 35 nm InGaAs mHEMT process and has dimensions of 1.5 mm×0.75 mm. It consists of a 50 µm GaAs substrate with a 1.7 µm thick Benzocyclobutene (BCB) layer on top in the area of the RF pads. Furthermore, the PA MMIC features two frontside and one backside gold (Au) metal layers (3.4 µm total frontside thickness and 2.7 µm backside thickness), resulting in a nominal MMIC thickness of 56 µm.

The LWA is based on a 50 µm InP substrate (dielectric constant, $\epsilon_r \approx 12.4$ and dielectric loss, $\tan\delta \leq 0.009$ at 300 GHz [37], [38]) with 1 µm thick top and bottom Au metal layers. A key component of the LWA is a grounded CPW leaky-wave unit cell with two mirrored L-slots in the lateral ground planes of the CPW, as shown in Fig. 2(a). The design procedure of the unit cell and the method used to optimize its dimensions are discussed in [16]. The dispersion characteristics of the unit cell are determined by its attenuation constant, i.e., the leakage rate (α), and phase constant of the first space harmonic causing radiation (β_{-1}). Furthermore, β_{-1} is derived from the phase constant of the fundamental guided CPW mode (β_0) and the grounded CPW leaky-wave unit cell length (p), as shown in equation (Eq.) 1. A relatively low α implies that the electromagnetic wave gradually leaks as it propagates along the LWA aperture, leading to high radiation efficiency. Furthermore, the value of β_{-1} determines the beam-steering angle of the LWA, as shown in Eq. 2, where λ_0 denotes the operating wavelength.

$$\beta_{-1} = \beta_0 - \left(\frac{2\pi}{p}\right) \tag{1}$$

$$\theta = \arcsin\left(\frac{\beta_{-1}}{2\pi\lambda_0}\right) \tag{2}$$

From Eq. 1 and Eq. 2, it can be interpreted that the beam-steering angle of the LWA (θ) depends on β_0, which in turn is proportional to $\sqrt{\epsilon_{eff}}$ (ϵ_{eff} denotes the CPW effective dielectric constant, which is directly related to the ϵ_r of the dielectric substrate [39]). Since the LWA is realized on a high dielectric constant substrate ($\epsilon_r \approx 12.4$), it helps in achieving a large beam-steering range for the LWA. An experimental validation of the influence of the dielectric constant on the beam-steering range of an LWA is shown in [40]. In addition, a high dielectric constant substrate also helps in realizing a compact antenna design, since LWAs are typically multiple guided wavelengths long [13]. Fig. 2(b) shows the α and β_{-1} of the leaky-wave unit cell, calculated using a method described in [16]. As seen in Fig. 2(b), the value of α is relatively low (≈ 0.3 Np/mm) throughout most of the operating frequency range. Additionally, the value of β_{-1} is negative from 220 GHz up to around 275 GHz, becomes 0 at around 275 GHz, and is positive from around 275 GHz to 325 GHz.

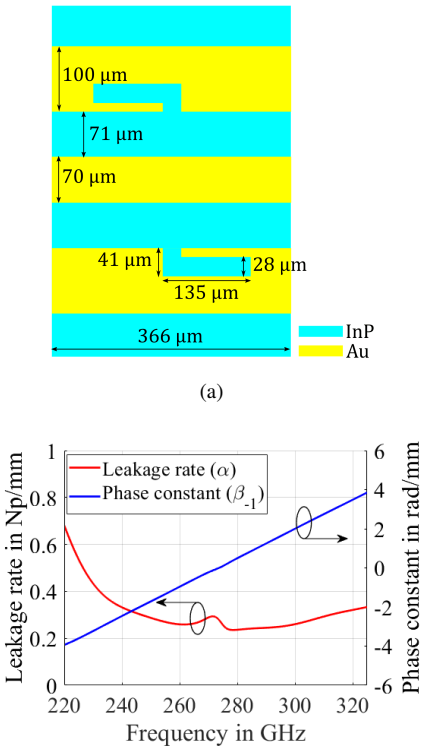

FIGURE 2: Grounded CPW leaky-wave unit cell (a) Top view of the unit cell with dimensions (b) Calculated leakage rate and phase constant of the unit cell [16].

According to Eq. 2, this implies that the beam-steering angle of the LWA is negative from 220 GHz to 275 GHz, indicating radiation in the backward quadrant. Around 275 GHz, the LWA radiates in the broadside direction, and from approximately 275 GHz to 325 GHz, the beam-steering angle becomes positive, indicating radiation in the forward quadrant. The LWA consists of a cascade of 16 grounded CPW leaky-wave unit cells, each with a length of 366 µm (i.e., approx. one guided wavelength at 275 GHz). According to Floquet's theory of periodic structures, Bloch waves propagate on the grounded CPW periodically loaded with leaky-wave unit cells. Therefore, a Bloch impedance (Z_B) is associated with the grounded CPW leaky-wave unit cell. The mirrored L-slots in the lateral ground planes of the grounded CPW leaky-wave unit cell reduce the impedance mismatch between the Z_B and the load impedance (Z_L=50 Ω) around the center frequency of 275 GHz, corresponding to broadside radiation of the LWA. This results in an improved reflection coefficient of the LWA within the operating frequency range of 220 GHz to 325 GHz. Furthermore, the mirrored L-slots mitigate the open stopband phenomenon, which tends to reduce the realized gain of a periodic LWA at its broadside radiation frequency of 275 GHz. A detailed description of this phenomenon is provided in [16].

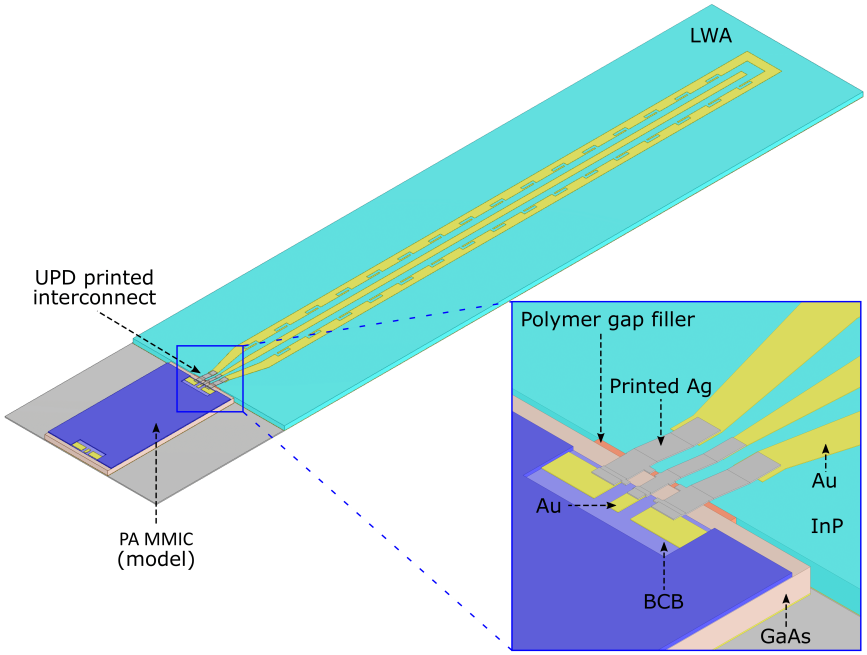

FIGURE 3: Simulation model of the PA MMIC (model with RF pads only) and the LWA with a UPD-printed interconnect.

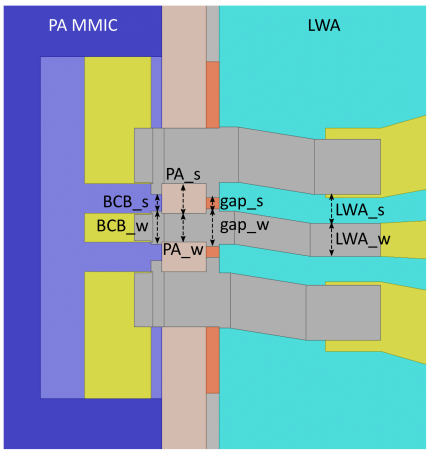

FIGURE 4: Dimensional parameters of the UPD-printed CPW interconnect between the PA MMIC and the LWA.

The cascade of 16 grounded CPW leaky-wave unit cells is terminated with a CPW open-circuit, in which the lateral ground plane terminals of the CPW leaky-wave structure are connected together, the CPW signal line is tapered, and it is terminated a short distance before the slot ends. LWAs realized at low frequencies are typically terminated with a matched load, so that as the leaky electromagnetic wave reaches the termination, the residual power is dissipated in the matched load to minimize reflections [41]. However, implementing a matched load termination in the high operating frequency range of 220 GHz to 325 GHz is not possible due to limitations in the manufacturing process used in this work. The CPW open-circuit termination used with the LWA helps in mitigating the parasitic fringing capacitance that exists at the open end of the CPW. A simulation analysis shown in [16] proves that this approach leads to an adequate impedance matching of the LWA across its operating frequency range. The measurement results of the LWA show that it operates from 220 GHz to 325 GHz, with a peak antenna gain of up to 13.5 dBi, and a beam-steering range of $-60°$ to $35°$. Furthermore, the LWA has a simulated total antenna efficiency of $\approx 82\%$ in the 220 GHz to 325 GHz range [16]. The LWA substrate has dimensions of $6.8\,\mathrm{mm} \times 1.8\,\mathrm{mm}$. The InP substrate of the LWA is very thin and relatively long. In addition, InP is more fragile than the GaAs substrate; therefore it is bonded to a 300 µm thick silicon wafer (i.e., carrier substrate, as shown in Fig. 1) using a thermocompression bonding process [16]. This, in turn, provides mechanical stability to the LWA, allowing it to be precisely placed next to the PA MMIC. A detailed process flow illustrating the fabrication of an InP LWA bonded to a silicon wafer is shown in [15]. This results in a total height of around 350 µm for the LWA.

To minimize insertion loss and connect the LWA and the PA MMIC with the shortest UPD-printed interconnect, it is essential to place the components as close together as possible and to compensate for the height difference between them. Taking this into consideration, the LWA and PA MMIC are positioned on a metal submount with a small edge-to-edge gap of 11 µm. This gap is filled with a polymer, NEA 123M with a stable $\epsilon_r \approx 3$ and $\tan\delta \approx 0.03$ in the target sub-THz range [42]. Furthermore, the LWA and the PA MMIC are placed on a submount with precisely milled steps, which effectively compensates for their height difference and ensures that the top Au metal layers of both the LWA and the PA MMIC are aligned at the same height.

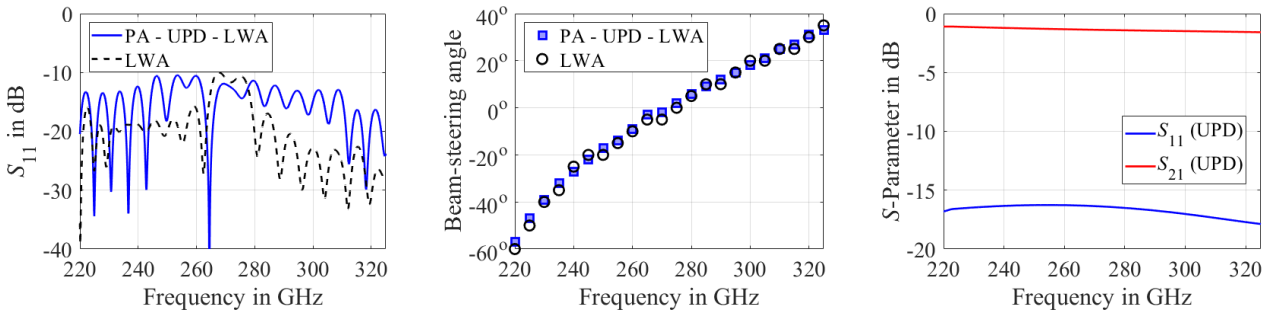

(a) (b) (c)

FIGURE 5: Simulation of the hybrid-integration assembly consisting of the PA MMIC (model with RF pads only), UPD-printed CPW interconnect, and the LWA, compared to the LWA alone with respect to the following: (a) Reflection coefficient (b) Beam-steering angle (c) Simulated S-parameter of the UPD-printed CPW interconnect using waveguide ports at the output RF pads of the PA MMIC and the input RF pads of the LWA.

The UPD-printed interconnect is based on a CPW transmission line that connects the RF output pads of the PA MMIC to the input pads of the LWA. The pads of both the PA MMIC and the LWA are in ground-signal-ground (GSG) configuration and have a characteristic impedance of $50\,\Omega$. To achieve broadband impedance matching for the UPD-printed CPW interconnect, it is designed to maintain a consistent characteristic impedance of $50\,\Omega$ across its entire length.

A simulation model of the PA MMIC and LWA with UPD-printed interconnect is shown in Fig. 3. The silicon-based carrier substrate is not included in the model, as it only provides mechanical stability for placing the LWA on the submount. Furthermore, it is electromagnetically isolated by the back metal ground plane of the LWA. The PA MMIC model includes only the RF pads. A zoomed view of the UPD-printed interconnect, also shown in Fig. 3, presents the stepped structure of the interconnect in greater detail. In this assembly, the UPD-printed CPW interconnect starts on the Au metal pads of the PA MMIC, crosses a thin BCB layer on GaAs, and then extends directly over the GaAs substrate until it reaches the edge of the PA MMIC. Thereafter, the UPD-printed CPW interconnect continues over a polymer gap filler onto the InP substrate of the LWA. Since each of these dielectric materials has a different dielectric constant, the physical dimensions of the UPD-printed CPW interconnect are adjusted depending on the dielectric constant of the substrate on which it is printed. Furthermore, the constraints of the UPD printing process, such as minimum feature sizes, gap sizes, and the pad layouts of the MMICs, are also considered to optimize the geometry of the interconnect. The dimensional parameters of the UPD-printed CPW interconnect between the PA MMIC and the LWA are shown in Fig. 4 and their values are listed in Table 1.

Two different simulations are conducted using CST Microwave Studio software. In the first simulation, only one waveguide port is set up at the output RF pads of the PA MMIC. The output RF pads of the PA MMIC are connected to the LWA via the UPD-printed CPW interconnect. The reflection coefficient (S_{11}) and the beam-steering angle obtained from the hybrid assembly simulation (marked as 'PA - UPD - LWA') are compared with those of the LWA itself, as shown in Fig. 5(a) and Fig. 5(b), respectively. In the frequency range from $220\,\mathrm{GHz}$ to $325\,\mathrm{GHz}$, the S_{11} of the hybrid assembly 'PA - UPD - LWA', similar to that of the LWA itself, is less than $-10\,\mathrm{dB}$, indicating good impedance matching between the RF pads of the PA MMIC, the UPD-printed interconnect, and the LWA. Additionally, the beam-steering angle of the hybrid assembly 'PA - UPD - LWA' steers its direction from $-57°$ to $33°$ as the frequency sweeps from $220\,\mathrm{GHz}$ to $325\,\mathrm{GHz}$. This is in good agreement with the LWA, whose beam-steering angle varies from $-60°$ to $35°$, as shown in Fig. 5(b). The beam of the LWA, and hence the beam of the hybrid assembly 'PA - UPD - LWA,' steers in only one dimension, i.e., along the elevation plane. In the second simulation, two waveguide ports on either side of the UPD-printed CPW interconnect are used; one port is at the edge of the output RF pads of the PA MMIC, and the other port is at the input RF pads of the LWA. The resulting reflection coefficient (S_{11}) and the transmission coefficient (S_{21}) are shown in Fig. 5(c). For this simulation, the realized dimensions according to Table 1 have been used. In the frequency range of $220\,\mathrm{GHz}$ to $325\,\mathrm{GHz}$, the simulated S_{11} is less than $-16\,\mathrm{dB}$, and the simulated S_{21} varies between $-1.1\,\mathrm{dB}$ and $-1.7\,\mathrm{dB}$.

III. Manufacturing

The UPD system operates as a direct-write technology, using a highly precise glass nozzle with an opening diameter of choice between 1.5 and $5\,\mu\mathrm{m}$, connected to an ink reservoir. A controllable pressure supply (up to $10\,\mathrm{bar}$) regulates the

TABLE 1: Target and realized dimensions of the UPD-printed interconnect between the PA MMIC and LWA.

	Target dim. (µm)	Realized dim. (µm)	Difference (µm)
BCB_w	30	29	-1
BCB_s	15	16	+1
PA_w	26	22	-4
PA_s	27	31	+4
gap_w	60	58	-2
gap_s	10	12	+2
LWA_w	30	28	-2
LWA_s	26	27	+1

FIGURE 6: A schematic of the UPD printing system nozzle and ink reservoir assembly.

extrusion of ink through the nozzle. A drawing of the system is shown in Fig. 6. For printing metallic structures, XTPL's standard CL85 silver nanoparticle ink is utilized because of its high solid content and viscosity. This helps reduce the substrate-ink interaction, which is an important factor in ensuring consistent results, given the range of materials (i.e., Au metal pads, BCB, GaAs, polymer gap filler, and InP) on which the CPW interconnect is printed in this assembly. The ink's thixotropic properties, due to its high solid content (82 wt.%), allow for printing with a high aspect ratio. The nozzle is positioned by a precision xyz-stage, while x- and y-axis cameras provide visual alignment and process monitoring. Maintaining contact between the nozzle and the substrate is essential for proper ink deposition, which poses a significant challenge on non-planar substrates.

Achieving uniform printed lines requires careful tuning of the velocity, acceleration, deceleration, and printing pressure. Since changes in printing pressure occur slowly, typically taking 1 to 2 seconds, it is necessary to compensate for the pressure variation by adjusting the printing speed proportionally. This ensures a consistent ink volume deposited per unit distance. This functionality is supported by the printer software through the "lineramp" command, which will be referenced later in this section. As mentioned in section II, a key objective of this work is to minimize the length of the UPD-printed CPW interconnect to reduce the insertion loss. This requires a precise alignment of the top surfaces of the PA MMIC and the LWA. To achieve this, the heights of both components are measured using a white light interferometer (WLI), and the metal submount shown in Fig. 1 is designed based on these measurements. The submount is manufactured by CNC machining of a tungsten-copper (CuW) block. CuW is chosen for the submount due to its linear coefficient of thermal expansion (CTE less than $7.5\times10^{-6}\mathrm{K}^{-1}$) [43], which closely matches that of the GaAs and InP substrates [44]. The CuW submount functions as a mechanical support, leveling structure, and ground connection for the PA MMIC. It is electroplated with a $2\,\mu\mathrm{m}$ Au layer to ensure high conductivity and prevent oxidation. The PA MMIC and the LWA are attached to the stepped structure of the CuW submount using an electrically conductive dicing die-attach film from Furukawa Electric [45].

The PA MMIC and the LWA are placed on the CuW submount using the FINEPLACER® femto 2, a system equipped with high-precision optical systems that enable die placement with sub-micrometer precision [46]. As previously mentioned, the PA MMIC and the LWA are to be placed as close together as possible so a short UPD-printed CPW interconnect can be manufactured for minimal insertion loss. A significant challenge in this task arises due to the $300\,\mu\mathrm{m}$ step in the submount at the edge of the PA MMIC, as shown in Fig. 1. The milling process results in a non-vertical step of the submount, which complicates the alignment of the PA MMIC and the LWA.

While the FINEPLACER® femto 2 provides near-perfect accuracy in automatic mode, it is still sensitive to human error in manual mode. The operator has erroneously chosen a slightly off-center structure on the PA MMIC to perform the alignment. Consequently, a $10\,\mu\mathrm{m}$ misalignment is observed between the RF signal pads of the PA MMIC and the LWA. This shift is also modeled in the CST simulation of the UPD-printed CPW interconnect shown in Fig. 4. It should be noted that in processes like flip-chip bonding, such an error could render the entire assembly unusable. However, the digital nature of printed interconnects allows for a simple compensation of this misalignment without compromising RF performance.

Although the submount is designed to compensate for the height difference between the PA MMIC and the LWA, ensuring that their top surfaces are at the same height, it is impossible to avoid some steps of a few µm in the surface topology. These steps occur between the Au metal pads and the surrounding area of the PA MMIC, as well as between the BCB-covered sections and the bare die areas of the PA MMIC. Additionally, the polymer-filled gap between the PA MMIC and the LWA introduces a minor change in surface height. A WLI measurement of the surface is shown in Fig. 7. Since UPD is a direct-write printing process, continuous contact is required between the printing nozzle

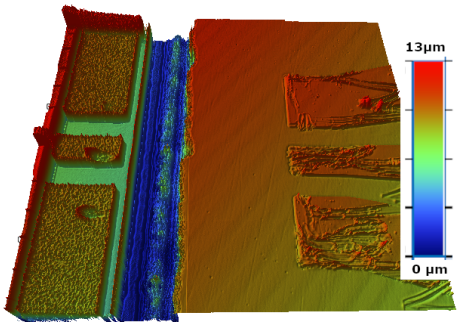

FIGURE 7: Surface topology of the PA MMIC and LWA assembly prior to printing, measured with a WLI. The Au Pads of the PA MMIC are visible on the left (red-green), surrounded by BCB (green), followed by the bare die area and the polymer-filled gap (both blue), and finally the InP LWA with Au pads on the right (red-green). Scratch marks from previous RF measurements can be seen on the pads.

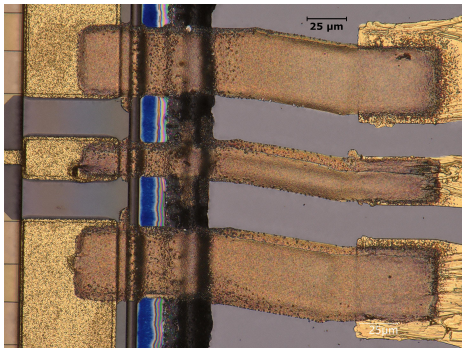

FIGURE 8: UPD-printed CPW interconnect between the PA MMIC and the LWA with a length of $185\,\mu\mathrm{m}$.

and the substrate. This requires 3D printing movements to accommodate the surface topology, a feature that the printer does not inherently provide. The manufacturer optimized the system for mostly planar surfaces or manually taught profiles, making it unsuitable for the complex topology of this assembly. This shortcoming of the UPD printing system is addressed by developing a process that allows surface measurement and the projection of printing paths onto the measured topography, thereby generating the necessary 3D printing movements. A WLI surface measurement is used, and the printing paths are manually adjusted for optimal precision. The printing is carried out at a pressure of $9.5\,\mathrm{bar}$ and a speed of $0.025\,\mathrm{mms}^{-1}$ using a $5\,\mu\mathrm{m}$ nozzle, resulting in a line width of $9\,\mu\mathrm{m}$. A line pitch of $3\,\mu\mathrm{m}$ is used to fill all surfaces. To ensure high uniformity in line segments, a custom, 3D-capable version of the "veclineramp" command (see above) is implemented for all printing movements. A $10\,\mu\mathrm{m}$ ramp-up and a $30\,\mu\mathrm{m}$ ramp-down distance, with a $20\,\mathrm{ms}$ start delay, are chosen. These short ramp distances were achievable due to the exceptionally high viscosity of the CL85 silver nanoparticle ink batch used, which allowed for a $5\,\mathrm{bar}$ non-printing pressure between consecutive line segments. The reduced pressure difference minimized adaptation time and, consequently, shortened the ramping distances. For segments shorter than the combined ramp-up and ramp-down distances, the printing pressure is reduced to $6\,\mathrm{bar}$ to prevent bulging in the printed lines.

When using the 3D projection method, precise leveling and alignment are essential to ensure that the printing start point matches the zero point in the projected printing paths. In this instance, both the printer and the WLI are leveled using a reference surface, and any digital leveling steps for the measured data are omitted. This approach ensures that all tilts and steps in the measurement data accurately correspond to the actual surface topology in the printer. Rotational alignment is achieved using features on the LWA. The corner of the LWA signal pad is chosen as the start point for printing, as it is clearly visible in both the printer and the measurement data, allowing for correct alignment.

Two layers of silver are printed, with a sintering step on a preheated hotplate at $250\,^{\circ}\mathrm{C}$ for $10\,\mathrm{min}$ after each layer. This process achieves a printed metal thickness of $2\,\mu\mathrm{m}$, which is also reflected in the CST simulation of UPD-printed CPW interconnects shown in section II. Fig. 8 shows the UPD printed CPW interconnect with both layers after sintering, demonstrating an alignment accuracy better than $3\,\mu\mathrm{m}$ between the printed structures, the PA MMIC, the LWA, and the two printed layers. The interconnect is printed with excellent dimensional accuracy. The realized dimensions of the different CPW segments are measured and compared with the target dimensions. The values of target and realized dimensions are shown in Table 1, and the structures corresponding to the names are shown in Fig. 4. The average deviation between the target and realized dimensions is $2.2\,\mu\mathrm{m}$, and the worst-case deviation is $4\,\mu\mathrm{m}$.

The final step of the assembly is adding the DC connections for the power supply of the PA MMIC. This is accomplished using standard wirebond technology. The DC supply PCB, the DC redistribution quartz chip, and die caps are attached to the same CuW submount as the PA MMIC and the LWA. A photograph of the assembly after bonding is shown in Fig. 9.

IV. Measurement Results and Analysis

Before measuring the hybrid-integration assembly of the PA MMIC and the LWA, the performance of the UPD-printed CPW interconnect needs to be experimentally validated by measuring its two-port S-parameters in the $220\,\mathrm{GHz}$ to $325\,\mathrm{GHz}$ range. It is important to note that if the two-port S-parameters of the UPD-printed CPW interconnect are measured in situ, i.e., by contacting two GSG probes positioned at the output RF pads of the PA MMIC and the input RF pads of the LWA, respectively, the active circuit of the PA MMIC and the UPD-printed CPW interconnect, was well as the input of the LWA and the interconnect would form a parallel configuration at the probe tip, thus resulting in

This article has been accepted for publication in IEEE Open Journal of Antennas and Propagation. This is the author's version which has not been fully edited and content may change prior to final publication. Citation information: DOI 10.1109/OJAP.2025.3551350

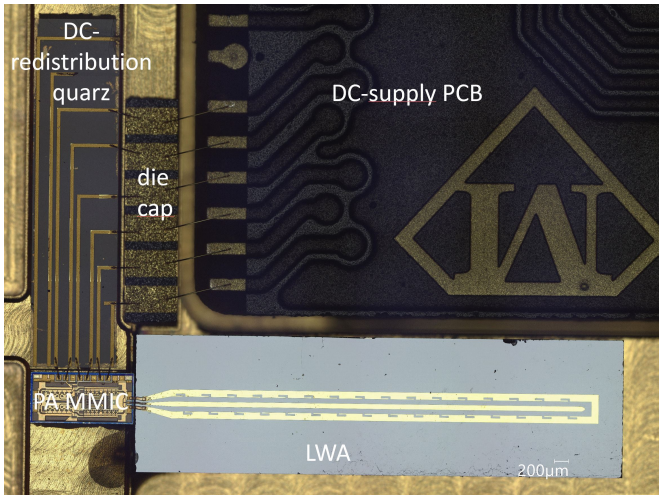

FIGURE 9: A photograph of the hybrid-integration assembly consisting of the PA MMIC and the LWA connected by UPD-printed CPW interconnect. A part of the DC-supply PCB (top right), DC redistribution chip (top left), and capacitors (top center) are also visible in the photo.

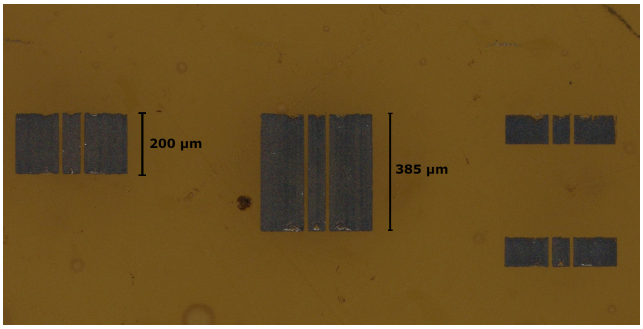

(a)

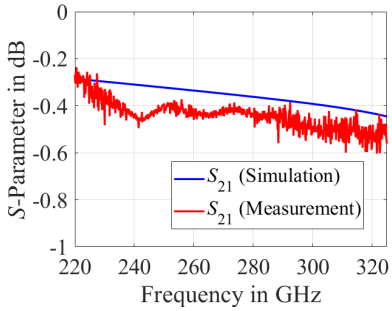

(b)

FIGURE 10: UPD-printed CPW test assembly (a) Microscope photo of the UPD-printed TRL calibration standards manufactured on a NEA 123M polymer substrate. (b) Measured and simulated S-parameters of a 185 µm long UPD-printed CPW manufactured on a NEA 123M polymer substrate.

severe mismatch for the two-port S-parameter measurement as well as potential destruction of the PA MMIC. To avoid that and to measure the true two-port S-parameters of a UPD-printed CPW in the 220 GHz to 325 GHz range, a test assembly is manufactured.

In this test assembly, the polymer used to fill the gap between the PA MMIC and the LWA (i.e., NEA 123M) is dispensed onto a metal sheet. The thickness of the polymer substrate is adjusted using a lapping procedure to ensure it is exactly the same as the thickness of the polymer gap filler used in the hybrid-integration assembly of the PA MMIC and the LWA. A UPD-printed CPW is manufactured on top of the polymer substrate such that its dimensions (i.e., CPW signal and slot width) match those shown in Fig. 4 and indicated in Table 1. The length of the UPD-printed CPW in this test assembly is 385 µm, whereas the length of the UPD-printed CPW interconnect used in the hybrid-integration assembly is 185 µm (see Fig. 8). Note that the length of the UPD-printed CPW in the test assembly is intentionally kept longer to minimize cross-talk between probes during a two-port S-parameter measurement. Furthermore, to extract the insertion loss of a 185 µm long UPD-printed CPW, through-reflect-line (TRL) calibration standards are also printed on the same polymer substrate, as shown in Fig. 10(a).

The two-port S-parameters of the UPD-printed CPW are measured using two waveguide probes with a GSG configuration and an 80 µm pitch, operating in the 220 GHz to 325 GHz range. A line-reflect-match (LRM) calibration is performed using an impedance standard substrate, followed by a second-tier TRL calibration using the TRL standards printed on the polymer substrate with UPD technology. This shifts the reference plane to the middle of the thru standard, after which a two-port S-parameter measurement of the UPD-printed CPW test assembly is performed. A simulation model of the test assembly -without the feeding CPW segments which are mathematically removed from the measurements by the second tier TRL calibration- is built, and an electromagnetic simulation is carried out using CST Microwave Studio software. The UPD-printed CPW test assembly shows excellent impedance matching, with a measured return loss greater than 30 dB throughout the 220 GHz to 325 GHz range. Furthermore, the simulated and measured insertion losses of the 185 µm long and 2 µm thick UPD-printed CPW test assembly are found to be in very good agreement, as shown in Fig. 10(b). The measured insertion loss varies between 0.3 dB and 0.6 dB in the 220 GHz to 325 GHz range. Furthermore, as shown in Section II, the evaluation of the UPD-printed CPW connecting the output RF pads of the PA MMIC and the input RF pads of the LWA leads to an insertion loss of 1.1 dB to 1.7 dB for the hybrid-integration assembly (see Fig. 5(c)). The approximately 1 dB difference in the insertion loss of the UPD-printed CPW used in the test assembly and the hybrid-integration assembly is attributed to the fact that, in the test assembly, the UPD-printed CPW is formed on a single polymer substrate,

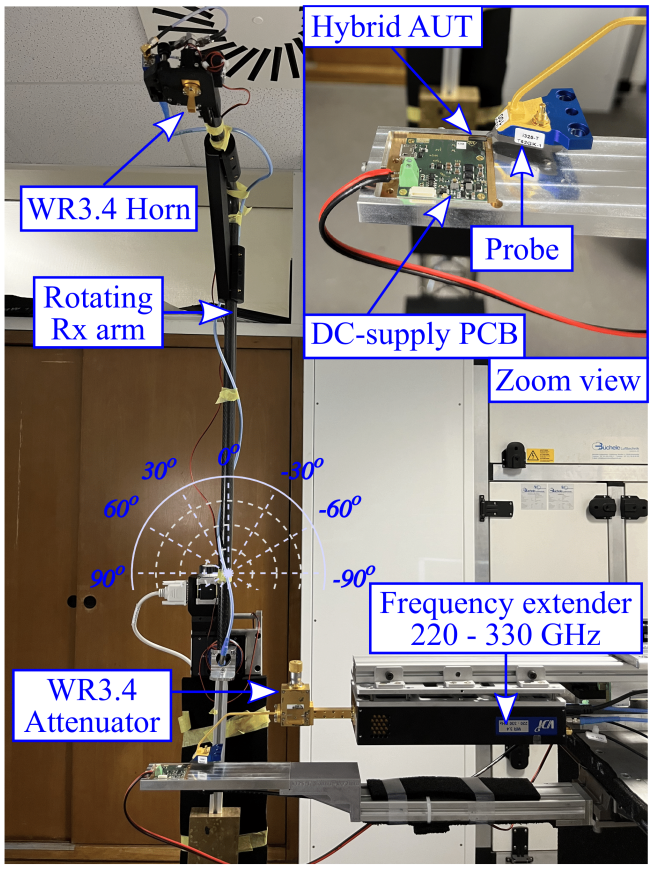

FIGURE 11: Probe-based measurement setup for the hybrid-integration assembly.

whereas in the hybrid-integration assembly, the UPD-printed CPW interconnect is manufactured over different substrates with different dielectric constants. This necessitates the manufacturing of various CPW dimensions to maintain a constant $50\,\Omega$ line impedance, a detailed description of which is provided in Section III, thus resulting in a slightly higher insertion loss for the UPD-printed CPW interconnect used in the hybrid-integration assembly.

The actual hybrid-integration assembly of the PA MMIC and the LWA with the UPD-printed CPW interconnect (i.e., Hybrid Assembly under Test, Hybrid AUT) is measured using a waveguide probe (Model: I325-T-GSG-100-BT) with a GSG configuration and a $100\,\mu\mathrm{m}$ pitch that operates in the WR3.4 frequency band of $220\,\mathrm{GHz}$ to $325\,\mathrm{GHz}$. The probe-based setup used for measuring the characteristics of the hybrid AUT is shown in Fig. 11. A detailed description of this antenna measurement setup and its working principle is provided in [47], [48]. In this setup, the Tx signal is generated by a two-port vector network analyzer (VNA) (Model: Keysight PNA-X Network Analyzer N5242B) combined with a millimeter-wave controller (Model: Keysight N5261A). The Tx signal generated by the VNA is fed to a frequency extender (Model: VDI WR3.4-VNAX) that provides standard frequency coverage from $220\,\mathrm{GHz}$ to

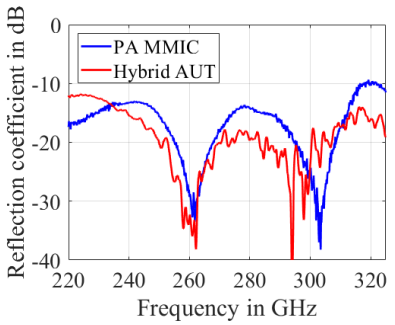

(a)

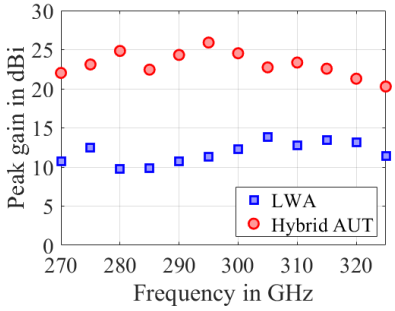

(b)

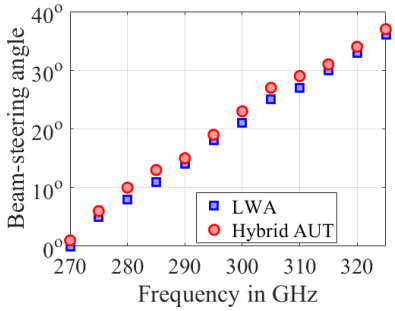

(c)

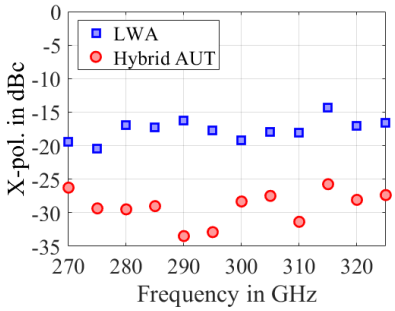

(d)

FIGURE 12: Measurement results of the hybrid-integration assembly (i.e., hybrid AUT) (a) Measured reflection coefficient of the hybrid AUT is compared with that of the PA MMIC alone. (b) Measured peak gain of the hybrid AUT is compared with that of the LWA alone. (c) Measured beam-steering angle of the hybrid AUT is compared with that of the LWA alone. (d) Measured cross-polarization of hybrid AUT is compared with that of the LWA alone.

This article has been accepted for publication in IEEE Open Journal of Antennas and Propagation. This is the author's version which has not been fully edited and content may change prior to final publication. Citation information: DOI 10.1109/OJAP.2025.3551350

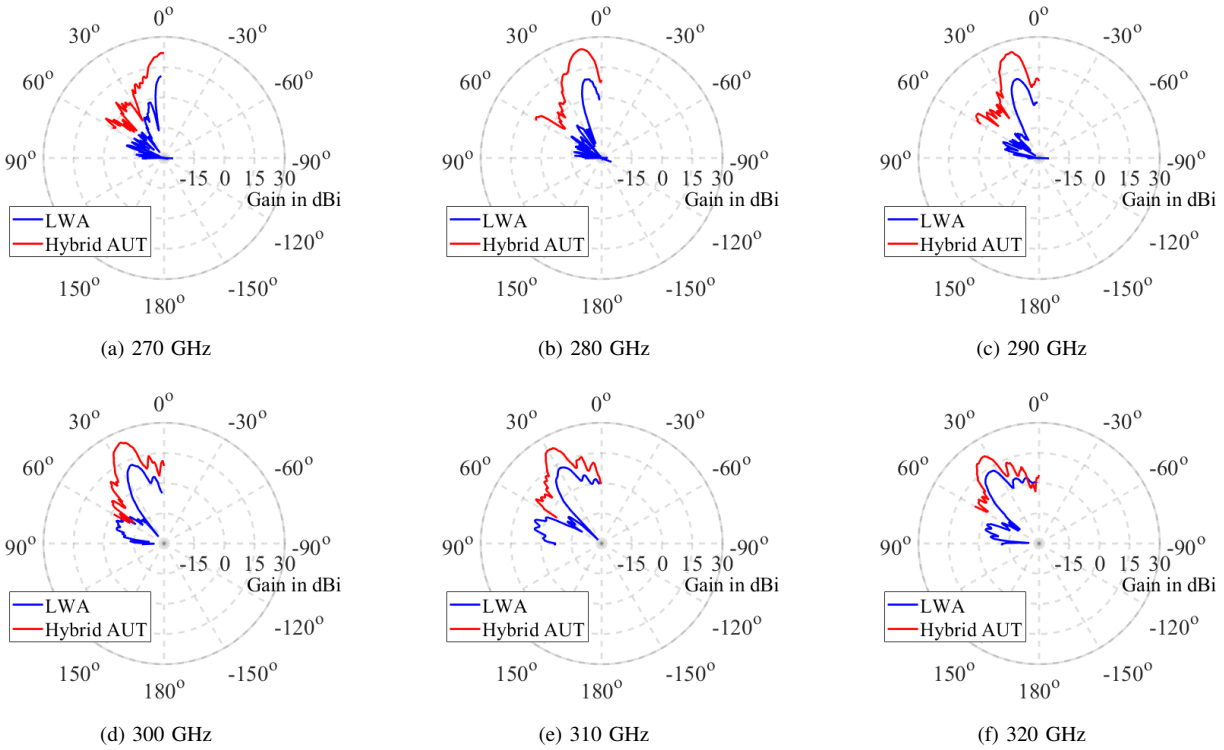

(a) 270 GHz (b) 280 GHz (c) 290 GHz

(d) 300 GHz (e) 310 GHz (f) 320 GHz

FIGURE 13: Measured far-field radiation patterns of the hybrid AUT are compared with those of the LWA alone in the beam-steering plane at frequencies (a) 270 GHz, (b) 280 GHz, (c) 290 GHz, (d) 300 GHz, (e) 310 GHz, and (f) 320 GHz.

330 GHz and a typical test port power of 1 dBm [49]. The test port of the frequency extender WR3.4-VNAX is connected to a WR3.4 waveguide attenuator, which in turn is connected to the probe. The waveguide attenuator provides an attenuation of approximately 6 dB and the typical insertion loss of the waveguide probe is 5.2 dB [50]. Consequently, the Tx signal has a power level of approximately -10 dBm at the probe tip. The probe contacts the hybrid AUT (i.e., the input RF pads of the PA MMIC placed at the feed end of the hybrid AUT). Therefore, the hybrid AUT serves as a Tx module in the probe-based measurement setup (see the zoom view in the inset of Fig. 11).

The receiver (Rx) module consists of a WR3.4 horn with a standard gain of 25 dBi and linear polarization, as specified by the manufacturer. The WR3.4 horn is connected to a WR3.4 down-conversion mixer, which is in turn connected to the second port of the VNA. The Rx module is mounted on a motorized rotational arm and is separated by a distance of 70 cm from the hybrid AUT, thus ensuring a far-field distance while measuring the radiation pattern of the hybrid AUT across the target frequency range. The hybrid AUT is precisely placed at the rotational center, and the Rx module arm is rotated around the hybrid AUT in the beam-steering plane (i.e., the plane parallel to the probe) to measure its two-dimensional far-field radiation pattern. As shown in section II, the hybrid AUT includes an LWA whose beam steers from $-57°$ to 33° as the frequency sweeps from 220 GHz to 325 GHz (see Fig. 5(b)). The far-field radiation pattern of the hybrid AUT is measured only in the forward quadrant (i.e., from 0° to 33°), corresponding to a frequency range of 270 GHz to 325 GHz. This is where the Rx module arm can be rotated in the cross-sectional plane parallel to the probe, with the hybrid AUT in its line of sight. On the other hand, the AUT radiation pattern in the backward quadrant (i.e., from $-57°$ to 0°), corresponding to a frequency range of 220 GHz to almost 270 GHz, is not measured, since when the Rx module is rotated in this sector of the cross-sectional plane parallel to the probe, it is shadowed by the measurement setup itself (i.e. probe, attenuator, and frequency extender). However, based on the experimental analysis of the UPD-printed CPW interconnect and the excellent match between the simulated and measured insertion loss over the complete target frequency range (see Fig. 10(b)), we can conclude that system integrity is maintained throughout the target frequency range of 220 GHz to 325 GHz, i.e., from $-57°$ to 0° in the 220 GHz to 270 GHz band and from 0° to 33° in the 270 GHz to 325 GHz band.

The probe-based measurement setup is calibrated before measuring the characteristics of the hybrid AUT. The calibration process begins with a one-port waveguide calibration performed at the output of the waveguide attenuator using a standard rectangular waveguide WR3.4 calibration kit.

The calibration standards consist of a waveguide short, a quarter-wave delay waveguide short, and a waveguide load. The calibration is performed from 220 GHz to 325 GHz with 801 frequency points and an IF bandwidth of 100 Hz. Subsequently, a gain calibration is performed by connecting a second standard-gain WR3.4 horn (25 dBi gain, linear polarization) to the waveguide attenuator. For the gain calibration, the Tx and Rx standard-gain WR3.4 horns are aligned with each other in two orthogonal cross-sectional planes, ensuring a perfect polarization match between the Tx and Rx WR3.4 horns. The forward transmission coefficient is measured to deduce the losses of the measurement setup, which are then used to calibrate the measured peak gain of the hybrid AUT. Finally, the probe tip is planarized, and a one-port impedance calibration is performed using short, open, and load standards from an impedance standard substrate (Model: P/N: 138-357) [51].

After calibrating the measurement setup, the reference plane is established at the probe tip. The hybrid AUT is then contacted with the probe, providing it with an RF input signal at a typical power level of -10 dBm (as described above). The reflection coefficient of the hybrid AUT is measured in the target frequency range of 220 GHz to 325 GHz and compared with the measured reflection coefficient of the PA MMIC itself. Note that in this case, the standalone PA MMIC is mounted on a submount and connected to the DC-supply PCB, DC redistribution chip, and capacitors using standard wire bonds. In other words, the standalone PA MMIC assembly is similar to the one shown in Fig. 9, the only difference being that the UPD-printed CPW interconnect and the LWA are not included in the standalone PA MMIC assembly. The PA MMIC is measured at a probe station by contacting both input and output RF pads with two waveguide probes (Model: I325-T-GSG-100-BT) configured in GSG with a 100 µm pitch. In this case, two-port S-parameters of the PA MMIC are measured, and the S-parameter measurement is preceded by a two-port Line-Reflect-Reflect-Match (LRRM) impedance calibration performed at the tip of each probe. The measured reflection coefficients of both the hybrid AUT and the PA MMIC show good agreement in the target frequency range, as shown in Fig. 12(a). This is expected because, as shown in Fig. 5(a), the RF output pads of the PA MMIC, the UPD-printed CPW interconnect, and the LWA exhibit good impedance matching in the target frequency range, and the measured reverse isolation of the PA MMIC is as high as 30 dB to 40 dB in this range.

Subsequently, the far-field radiation pattern of the hybrid AUT is measured from 270 GHz to 325 GHz in steps of 5 GHz. (As explained above, measuring the far-field radiation pattern in the lower frequency range of 220 GHz to almost 270 GHz is not possible due to restrictions imposed by the measurement setup.) These far-field radiation pattern measurements are used to determine the peak gain and the beam-steering angle of the hybrid AUT. The measured peak gain and beam-steering angle of the hybrid AUT are compared with those of a standalone LWA, as shown in Fig. 12(b) and Fig. 12(c), respectively. The measured beam-steering angle of the hybrid AUT matches that of the standalone LWA, demonstrating that the beam-steering functionality of the LWA is not distorted by the hybrid integration of the PA MMIC with the UPD-printed CPW interconnect.

Upon comparing the measured peak gain of the hybrid AUT and the LWA, it is observed that the hybrid AUT shows an average gain enhancement of up to 15 dB in the frequency range of 270 GHz to 325 GHz relative to the LWA. Furthermore, Fig. 12(d) compares the measured cross-polarization (X-pol.) of the hybrid AUT with that of the LWA alone. The X-pol. level is shown with respect to the corresponding measured peak gain of the LWA and the Hybrid AUT (i.e., dBc) in the 270 GHz to 325 GHz range. The X-pol. of the LWA lies between -14 dBc and -20 dBc, whereas the X-pol. of the Hybrid AUT lies between -26 dBc and -34 dBc. The X-pol. level of the Hybrid AUT is up to 14 dB lower than that of the LWA, which is consistent with the average difference in their measured peak gain values shown in Fig. 12(b). Therefore, it can be concluded that the absolute X-pol. level of the Hybrid AUT is nearly the same as that of the LWA. In other words, the hybrid assembly presented in this work does not degrade the X-pol. level of the LWA and keeps it intact. The on-wafer measurements of the PA MMIC show variation in the measured gain depending on the RF input signal power. The on-wafer measurements corresponding to RF input signal powers of -15 dBm and -10 dBm show a reduction in the measured gain from 23 dB to 20 dB at 270 GHz [21]. Due to the typical RF input signal power of -10 dBm available in the measurement setup of the hybrid AUT, a similar behavior is expected at higher frequencies; therefore, the gain of the PA MMIC is around 17 dB from 270 GHz to 325 GHz. Additionally, in contrast to the on-wafer measurement of the PA MMIC, where the DC bias is directly provided using a multi-contact DC probe, in the hybrid AUT, the DC bias is supplied by connecting the PA MMIC to a DC-supply PCB, a DC redistribution chip, and capacitors using standard wire bonds. This leads to a further gain reduction of approximately 1 dB, which was verified in the S-parameter measurements of the stand alone PA MMIC. Finally, the simulated insertion loss of the UPD-printed CPW interconnect is up to 1.7 dB, as shown in Fig. 5(c). Taking these factors into consideration, the measured peak gain of up to 26 dBi achieved by the hybrid AUT is found to be justified. The far-field radiation patterns measured in the beam-steering plane of the hybrid AUT and the standalone LWA at frequencies of 270 GHz, 280 GHz, 290 GHz, 300 GHz, 310 GHz and 320 GHz are shown in Fig. 13. As seen in these polar plots, the hybrid AUT exhibits the same beam-steering range and a significant gain enhancement of up to 15 dB compared to the LWA.

A comparison with prior works on hybrid-integration assemblies operating in the 220 GHz to 325 GHz range is shown in Table 2. The hybrid AUT presented in this work

exhibits a lower assembly loss over a broad sub-THz range compared to previous works. Moreover, the hybrid AUT also achieves a very high peak gain and a low side lobe level (SLL) with a compact hybrid-integration assembly (i.e., without using a lens).

V. CONCLUSION AND OUTLOOK

This paper presents the first hybrid-integration assembly of a PA MMIC and a beam-steering LWA using a UPD-printed CPW interconnect, operating in the broadband sub-THz range of 220 GHz to 325 GHz. In this assembly, a 35 nm InGaAs mHEMT PA with a saturated output power of up to 14.5 dBm and an InP LWA with a peak gain of up to 13.5 dBi and a beam-steering range from $-60°$ to $35°$ are used. The PA MMIC and the LWA are mounted on a submount with a precisely milled stepped structure that compensates for the height difference of ≈300 µm between the PA MMIC and the LWA. Using the FINEPLACER® femto 2, a system equipped with high-precision optical systems enabling sub-µm die placement, the PA MMIC and the LWA are positioned at an edge-to-edge distance of merely 11 µm. This small gap is filled with a polymer, NEA 123M, with a stable dielectric constant in the target sub-THz range.

The UPD-printing technique is employed to print a CPW interconnect between the PA MMIC and the LWA. Since the interconnect is printed on various dielectric materials, including BCB, GaAs, polymer gap filler, and InP, which have different dielectric constants and thicknesses, the geometry of the interconnect is optimized to ensure a consistent characteristic impedance of 50 Ω across its length, thus ensuring good impedance matching over the target sub-THz range. A WLI is used to measure the surface height with very high precision, based on which the UPD printing path is optimized. The UPD-printed interconnect also compensates for slight misalignments between the signal pads of the PA MMIC and the LWA. The realized dimensions of the UPD-printed interconnect are measured and compared with the target dimensions and a worst-case deviation of 4 µm is observed. The manufacturing tolerances of the interconnect, including the thickness of the printed metal, the slight misalignment between the PA MMIC and LWA pads, and the measured dimensions, are incorporated into the simulation model of the UPD-printed interconnect. The simulated S-parameters of the interconnect show an insertion loss of up to 1.7 dB in the target sub-THz range. The reliability of the simulation model is verified through the manufacturing and measurement of a UPD-printed CPW test assembly which shows very good agreement with the simulation model. A DC-supply PCB, DC redistribution chip, and capacitors are also mounted on the submount and connected to the PA MMIC using wire bonds.

A probe-based setup is used to measure the characteristics of the hybrid AUT. The measured reflection coefficient of the hybrid AUT is less than -10 dB from 220 GHz to 325 GHz. The peak gain and beam-steering angle of the hybrid AUT are measured from 270 GHz to 325 GHz, as measurements at lower frequencies are restricted by the measurement setup. From 270 GHz to 325 GHz, the hybrid AUT achieves a measured peak gain of up to 26 dBi, demonstrating a gain enhancement of up to 15 dB compared to the LWA. The measured SLL of the hybrid AUT is 13.5 dB less than the peak gain and the simulated radiation efficiency is around 65% at 295 GHz. The cross-polarization of the hybrid AUT has been measured and it lies between -26 dBc and -34 dBc. The factors influencing the gain enhancement achieved by the hybrid AUT are carefully analyzed. This includes the RF input signal power available at the probe tip, the DC-supply PCB, DC redistribution chip, and capacitors connected via wire bonds to the DC input pads of the PA MMIC, and the insertion loss of the UPD-printed interconnect.

The measured beam-steering angle of the hybrid AUT varies from $0°$ to $37°$ as the frequency sweeps from 270 GHz to 325 GHz, which closely matches the LWA. The successful demonstration of the hybrid integration assembly of a PA MMIC and LWA in the 220 GHz to 325 GHz range opens two key prospects for future 6G wireless systems. First, this hybrid assembly can be integrated with a sub-THz Tx chip (e.g., VCO, frequency multiplier) to realize a beam-steering Tx RF frontend. This Tx frontend can be used in a sub-THz point-to-multipoint wireless link that extends over several meters, enabling simultaneous high-data-rate transmissions to multiple users. Second, the successful demonstration of UPD printing to connect an active MMIC and an antenna highlights the precision and flexibility of this printing technique. The ability to optimize the UPD printing path according to the dielectric constants and surface heights of heterogeneous chips, combined with the low insertion loss of a UPD-printed interconnect in the sub-THz range, demonstrates its suitability for future sub-THz system-on-package integration. Consequently, UPD printing can also be employed in the next step: integrating a sub-THz Tx chip with this hybrid assembly. This advancement will result in an extremely compact sub-THz Tx RF frontend, making it highly attractive for future 6G wireless systems.

Author contribution

The conceptualization of this work was done by Georg Gramlich and Akanksha Bhutani. The design and manufacturing of the assembly were carried out by Georg Gramlich. Measurements were conducted by Elizabeth Bekker, Joel Dittmer, and Akanksha Bhutani. Martin Roemhild and Holger Baur contributed to the optimization of the printing and sintering processes under the supervision of Norbert Fruehauf. Fabian Thome, Axel Tessmann, and Michael Kuri designed, tested, and provided the PA-MMIC and the DC-PCB. Luca Valenziano manufactured the wirebond interconnects between the PA-MMIC and the DC-supply PCB. Tom Neerfeld manufactured the LWA based on a specialized InP process developed under the supervision of Andreas Stöhr. The paper was written by Georg Gramlich and Akanksha

TABLE 2: Comparison with prior works on hybrid-integration assemblies operating in the 220 GHz to 325 GHz range.

Hybrid AUT	MMIC	Antenna	Frequency (GHz)	Integration technique	Assembly loss (dB)	Peak gain (dBi)	SLL (dB)	Ref.
MMIC-Antenna	InGaAs PA	InP LWA	220 - 325	UPD-printed CPW	1.1 - 1.7	26	-13.5	**This work**
MMIC-Antenna	GaAs x36 Multiplier	Quartz stacked patch + Lens	280 - 310	Single wirebond	3 - 4	5 (w/o lens), 23 (w. lens)	-9	[22]
MMIC-Antenna	SiGe BiCMOS BPSK Tx	PCB antenna	230 – 255	Differential wirebond	<6	6	-	[23]
MMIC-Antenna	GaAs Balun	Quartz-cavity LW feed + Lens	220 - 320	Air-bridge differential interconnect	2.1 - 2.7[a]	≈15 (w/o lens), 25 (w. lens)	-	[25]
MMIC-Antenna	THz Amplifier[b]	Elevated slot antenna	274[c]	Printed CPW via multi-photon laser lithography	<2	5.5	-	[29]
MMIC-MMIC	InP and Si MMICs	n/a	up to 300	CPW based on wafer-level packaging	<4	n/a	n/a	[26]

[a]For 730 µm long feed line, excluding the loss of lens and polarization mismatch.
[b]The amplifier MMIC is not connected to the antenna, during the antenna measurement.
[c]Antenna bandwidth not given in the paper.

Bhutani. Sebastian Randel, Christian Koos, Thomas Zwick, and Akanksha Bhutani acquired funding for this project. Overall supervision and coordination of this work were provided by Akanksha Bhutani.

References

[1] T. S. Rappaport, Y. Xing, O. Kanhere, *et al.*, "Wireless communications and applications above 100 ghz: Opportunities and challenges for 6g and beyond," *IEEE Access*, vol. 7, pp. 78 729–78 757, 2019. DOI: 10.1109/ACCESS.2019.2921522.

[2] Y. Morishita, T. Teraoka, Y. Kashino, *et al.*, "300-ghz-band self-heterodyne wireless system for real-time video transmission toward 6g," in *2020 IEEE International Symposium on Radio-Frequency Integration Technology (RFIT)*, 2020, pp. 151–153. DOI: 10.1109/RFIT49453.2020.9226182.

[3] ITU-R, *Future technology trends of terrestrial international mobile telecommunications systems towards 2030 and beyond*, https://www.itu.int/pub/R-REP-M.2516, Accessed: Oct. 02, 2024, 2022.

[4] V. Petrov, T. Kurner, and I. Hosako, "Ieee 802.15.3d: First standardization efforts for sub-terahertz band communications toward 6g," *IEEE Communications Magazine*, vol. 58, no. 11, pp. 28–33, 2020. DOI: 10.1109/MCOM.001.2000273.

[5] ITU-R, *Attenuation by atmospheric gases", recommendation itu-r p.676-11*, https://www.itu.int/dms_pubrec/itu-r/rec/p/R-REC-P.676-11-201609-I!!PDF-E.pdf, Accessed: Oct. 02, 2024, 2016.

[6] I. Dan, G. Ducournau, S. Hisatake, P. Szriftgiser, R.-P. Braun, and I. Kallfass, "A terahertz wireless communication link using a superheterodyne approach," *IEEE Transactions on Terahertz Science and Technology*, vol. 10, no. 1, pp. 32–43, 2020. DOI: 10.1109/TTHZ.2019.2953647.

[7] D. Zhao, P. Gu, J. Zhong, *et al.*, "Millimeter-wave integrated phased arrays," *IEEE Transactions on Circuits and Systems I: Regular Papers*, vol. 68, no. 10, pp. 3977–3990, 2021, blue-highlight. DOI: 10.1109/TCSI.2021.3093093.

[8] P. Sanjari and F. Aflatouni, "An integrated photonic-assisted phased array transmitter for direct fiber to mm-wave links," *Nature Communications*, vol. 14, no. 1414(2023), pp. 1–11, 14, blue-highlight. DOI: https://doi.org/10.1038/s41467-023-37103-w.

[9] Y. Kim, S. Kim, I. Lee, M. Urteaga, and S. Jeon, "A 220–320-ghz vector-sum phase shifter using single gilbert-cell structure with lossy output matching," *IEEE Transactions on Microwave Theory and Techniques*, vol. 63, no. 1, pp. 256–265, 2015, blue-highlight. DOI: 10.1109/TMTT.2014.2376515.

[10] X. Fu, F. Yang, C. Liu, X. W. Wu, and T. J. Cui, "Terahertz beam steering technologies: From phased arrays to field-programmable metasurfaces," *Advanced Optical Materials*, vol. 8, no. 1900628, pp. 1–22, 2020. DOI: https://doi.org/10.1002/adom.201900628.

[11] Y. Monnai, X. Lu, and K. Sengupta, "Terahertz beam steering: From fundamentals to applications," *Journal of Infrared, Millimeter, and Terahertz Waves*, vol. 44, 169–211, 2023. DOI: https://doi.org/10.1007/s10762-022-00902-1.

[12] J. Dittmer, A. Bhutani, F. Beuthan, *et al.*, "Multi-user long-distance sub-thz wireless communication," *IEEE Transactions on Terahertz Science and Technology*, pp. 1–11, 2025, blue-highlight. DOI: 10.1109/TTHZ.2025.3530757.

[13] A. A. Oliner, "Antenna engineering handbook," in USA: McGraw-Hill, Inc., 1993, ch. Leaky-Wave Antennas, pp. 10–1 –10–33.

[14] B. Gashi, D. Meier, L. John, *et al.*, "Broadband 400 ghz on-chip antenna with a metastructured ground plane and dielectric resonator," *IEEE Transactions on Antennas and Propagation*, vol. 70, no. 10, pp. 9025–9038, 2022. DOI: 10.1109/TAP.2022.3177527.

[15] P. Lu, T. Haddad, B. Sievert, *et al.*, "Inp-based thz beam steering leaky-wave antenna," *IEEE Transactions on Terahertz Science and Technology*, vol. 11, no. 2, pp. 218–230, 2021. DOI: 10.1109/TTHZ.2020.3039460.

[16] A. Bhutani, M. Kretschmann, J. Dittmer, P. Lu, A. Stöhr, and T. Zwick, "A 220 ghz to 325 ghz grounded coplanar waveguide based periodic leaky-wave beam-steering antenna in indium phosphide process," *Electronics*, vol. 12, no. 16, 2023, ISSN: 2079-9292. DOI: 10.3390/electronics12163482. [Online]. Available: https://www.mdpi.com/2079-9292/12/16/3482.

[17] K. Sarabandi, A. Jam, M. Vahidpour, and J. East, "A novel frequency beam-steering antenna array for submillimeter-wave applications," *IEEE Transactions on Terahertz Science and Technology*, vol. 8, no. 6, pp. 654–665, 2018, blue-highlight. DOI: 10.1109/TTHZ.2018.2866019.

[18] H. Guerboukha, R. Shrestha, J. Neronha, *et al.*, "Efficient leaky-wave antennas at terahertz frequencies generating highly directional beams," *Applied Physics Letters*, vol. 117, no. 26, p. 261 103, Dec. 2020, blue-highlight, ISSN: 0003-6951. DOI: 10.1063/5.0033126. eprint: https://pubs.aip.org/aip/apl/article-pdf/doi/10.1063/5.0033126/19755003/261103_1_online.pdf. [Online]. Available: https://doi.org/10.1063/5.0033126.

[19] H. Guerboukha, R. Shrestha, J. Neronha, Z. Fang, and D. M. Mittleman, "Conformal leaky-wave antennas for wireless terahertz communications," *Nature : Communications Engineering*, vol. 2, no. 17 (2023), pp. 1–9, 2023, blue-highlight. [Online]. Available: https://doi.org/10.1038/s44172-023-00067-2.

[20] W. Fuscaldo, S. Tofani, D. C. Zografopoulos, *et al.*, "Systematic design of thz leaky-wave antennas based on homogenized metasurfaces," *IEEE Transactions on Antennas and Propagation*, vol. 66, no. 3, pp. 1169–1178, 2018, blue-highlight. DOI: 10.1109/TAP.2018.2794393.

[21] F. Thome and A. Leuther, "Low-noise power-amplifier mmics for the wr4.3 and wr3.4 bands in a 35-nm gate-length ingaas mhemt technology," *IEEE Microwave and Wireless Technology Letters*, vol. 34, no. 6, pp. 749–752, 2024. DOI: 10.1109/LMWT.2024.3388320.

[22] A. Dyck, M. Rösch, A. Tessmann, *et al.*, "A transmitter system-in-package at 300 ghz with an off-chip antenna and gaas-based mmics," *IEEE Transactions on Terahertz Science and Technology*, vol. 9, no. 3, pp. 335–344, 2019. DOI: 10.1109/TTHZ.2019.2910511.

[23] J. Hebeler, L. Steinweg, F. Ellinger, and T. Zwick, "Performance evaluation of ultra-wideband 246-ghz bpsk transmitters on an organic substrate with external chip and substrate antenna," *IEEE Transactions on Microwave Theory and Techniques*, vol. 72, no. 10, pp. 6153–6163, 2024. DOI: 10.1109/TMTT.2024.3390055.

[24] J. Hebeler, L. Steinweg, and T. Zwick, "Differential bondwire interface for chip-to-chip and chip-to-antenna interconnect above 200 ghz," in *2022 52nd European Microwave Conference (EuMC)*, 2022, pp. 306–309. DOI: 10.23919/EuMC54642.2022.9924340.

[25] M. Arias Campo, K. Holc, R. Weber, *et al.*, "H-band quartz-silicon leaky-wave lens with air-bridge interconnect to gaas front-end," *IEEE Transactions on Terahertz Science and Technology*, vol. 11, no. 3, pp. 297–309, 2021. DOI: 10.1109/TTHZ.2021.3049640.

[26] Y. Araki, Y. Shiratori, H. Hamada, *et al.*, "A low-loss dc-to-300 ghz inp/si interconnection based on wafer level packaging using chip-first/facedown process," in *2024 IEEE/MTT-S International Microwave Symposium - IMS 2024*, 2024, pp. 816–819. DOI: 10.1109/IMS40175.2024.10600247.

[27] W. Spain, Z. Darpinian, C. Crump, J. Papapolymerou, P. Chahal, and J. D. Albrecht, "Fully aerosol jet printed interconnects and fill materials for millimeter wave circuits," in *2021 IEEE International Conference on Microwaves, Antennas, Communications and Electronic Systems (COMCAS)*, 2021, pp. 107–110. DOI: 10.1109/COMCAS52219.2021.9629010.

[28] M. Ihle, S. Ziesche, C. Zech, and B. Baumann, "Functional printing of mmic-interconnects on ltcc packages for sub-thz applications," in *2019 22nd European Microelectronics and Packaging Conference & Exhibition (EMPC)*, 2019, pp. 1–4. DOI: 10.23919/EMPC44848.2019.8951799.

[29] P. Maier, A. Kotz, J. Hebeler, *et al.*, *Freeform terahertz structures fabricated by multi-photon lithography and metal coating*, 2024. arXiv: 2401.03316 [physics.optics]. [Online]. Available: https://arxiv.org/abs/2401.03316.

[30] G. Gramlich, M. Roemhild, H. Baur, *et al.*, "Ultra-precise deposition (upd) printing for millimeter wave interconnects in d-band," in *2023 Asia-Pacific Microwave Conference (APMC)*, 2023, pp. 1–3. DOI: 10.1109/APMC57107.2023.10439807.

[31] L. Valenziano, F. Zeh, G. Gramlich, T. Zwick, and A. Bhutani, "Ultra-precise deposition – xtpl technology for 3d printed broadband spiral inductors," in *2024 15th German Microwave Conference (GeMiC)*, 2024, pp. 53–56. DOI: 10.23919/GeMiC59120.2024.10485325.

[32] L. Valenziano, G. Gramlich, A. Quint, T. Zwick, and A. Bhutani, "3d printing of interdigitated finger capacitors using ultra-precise deposition technology," in *2024 25th International Microwave and Radar Conference (MIKON)*, 2024, pp. 26–30. DOI: 10.23919/MIKON60251.2024.10633928.

[33] M. Łysień, Ł. Witczak, A. Wiatrowska, *et al.*, "High-resolution deposition of conductive and insulating materials at micrometer scale on complex substrates," *Scientific reports*, vol. 12, no. 1, p. 9327, 2022, blue-highlight. DOI: 10.1038/s41598-022-13352-5.

[34] F. Cai, Y.-h. Chang, K. Wang, C. Zhang, B. Wang, and J. Papapolymerou, "Low-loss 3-d multilayer transmission lines and interconnects fabricated by additive manufacturing technologies," *IEEE Transactions on Microwave Theory and Techniques*, vol. 64, no. 10, pp. 3208–3216, 2016, blue-highlight, ISSN: 0018-9480. DOI: 10.1109/TMTT.2016.2601907.

[35] S. A. Nauroze, J. G. Hester, B. K. Tehrani, *et al.*, "Additively manufactured rf components and modules: Toward empowering the birth of cost-efficient dense and ubiquitous iot implementations," *Proceedings of the IEEE*, vol. 105, no. 4, pp. 702–722, 2017, blue-highlight, ISSN: 0018-9219. DOI: 10.1109/JPROC.2017.2658565.

[36] M. Roemhild, G. Gramlich, J. Wendel, H. Baur, T. Zwick, and N. Fruehauf, "Ultraprecise printing of d-band interconnects using dielectric ramps," in *2024 15th German Microwave Conference (GeMiC)*, 2024, pp. 57–60. DOI: 10.23919/GeMiC59120.2024.10485303.

[37] J. A. Hejase, P. R. Paladhi, and P. P. Chahal, "Terahertz characterization of dielectric substrates for component design and nondestructive evaluation of packages," *IEEE Transactions on Components, Packaging and Manufacturing Technology*, vol. 1, no. 11, pp. 1685–1694, 2011, blue-highlight. DOI: 10.1109/TCPMT.2011.2163632.

[38] Michigan State University, East Lansing, MI 48824, *Indium phosphide*, https://www.egr.msu.edu/~tesla-web/tesla/TESLA/inorganic.html [Accessed: (05.12.2024)], blue-highlight, 2011.

[39] R. N. Simons, "Coplanar waveguide circuits, components, and systems," in USA: John Wiley Sons, Inc., 2001, ch. Conductor-Backed Coplanar Waveguide, pp. 87 –109, blue-highlight.

[40] K. Neophytou, S. Iezekiel, M. Steeg, and A. Stöhr, "Design of pcb leaky-wave antennas for wide angle beam steering," in *2018 11th German Microwave Conference (GeMiC)*, blue-highlight, 2018, pp. 152–155. DOI: 10.23919/GEMIC.2018.8335052.

[41] D. R. Jackson, C. Caloz, and T. Itoh, "Leaky-wave antennas," *Proceedings of the IEEE*, vol. 100, no. 7, pp. 2194–2206, 2012, blue-highlight. DOI: 10.1109/JPROC.2012.2187410.

[42] G. Gramlich, K. Speder, M. Roernhild, *et al.*, "Dielectric characterization of adhesives for thz packaging in wr6.5, wr3.4 and wr2.2 bands," in *2024 18th European Conference on Antennas and Propagation (EuCAP)*, 2024, pp. 1–5. DOI: 10.23919/EuCAP60739.2024.10501389.

[43] W. S. G. C. KG, *Data sheet tungsten-copper (wcu) [also: Coppertungsten cuw]*, https://www.whs-sondermetalle.de/images/pdf/WCu-Tungsten-Copper.pdf [Accessed: (17.10.2024)], 2024.

[44] T. Soma, J. Satoh, and H. Matsuo, "Thermal expansion coefficient of gaas and inp," *Solid State Communications*, vol. 42, no. 12, pp. 889–892, 1982, ISSN: 0038-1098. DOI: https://doi.org/10.1016/0038-1098(82)90233-2. [Online]. Available: https://www.sciencedirect.com/science/article/pii/0038109882902332.

[45] L. Furukawa Electric Co., *Electrically/thermally conductive dicing die attach film*, https://www.furukawa.co.jp/uvtape/en/technology/cdaf.html [Accessed: (17.10.2024)], 2024.

[46] F. G. C. KG, *Advanced automatic sub-micron bonder*, https://finetech.de/products/fineplacer-femto-2/ [Accessed: (17.10.2024)], 2024.

[47] H. Gulan, S. Beer, S. Diebold, *et al.*, "Probe based antenna measurements up to 325 ghz for upcoming millimeter-wave applications," in *2013 International Workshop on Antenna Technology (iWAT)*, 2013, pp. 228–231. DOI: 10.1109/IWAT.2013.6518338.

[48] S. Beer and T. Zwick, "Probe based radiation pattern measurements for highly integrated millimeter-wave antennas," in *Proceedings of the Fourth European Conference on Antennas and Propagation*, 2010, pp. 1–5.

[49] I. Virginia Diodes, *Vna extender - vdi model: Wr3.4-vnax*, https://www.vadiodes.com/en/wr3-4vnax [Accessed: (17.10.2024)], 2024.

[50] I. Formfactor, *Probe selection guide*, https://www.formfactor.com/download/probe-selection-guide/?wpdmdl=2561\&refresh=67175034296b31729581108 [Accessed: (17.10.2024)], 2024.

[51] I. Formfactor, *Cascade impedance standard substrate map*, https://www.formfactor.com/download/iss-map-138-357/?wpdmdl=3179 [Accessed: (17.10.2024)], 2024.

Georg Gramlich (Student Member, IEEE) received the master's degree in electrical engineering from the Karlsruhe Institute of Technology (KIT), Karlsruhe, Germany, in 2019, and the French Diplôme d'Ingénieur degree from the Grenoble Institute of Engineering (INP), Grenoble, France, in 2019.He is currently working as a Research Associate with the Institute of Radio Frequency Engineering and Electronics (IHE), KIT. His main research interest is on printing technologies - notably Aerosol Jet and UPD Printing - for radio frequency electronics. He specializes on printed interconnects.

Elizabeth Bekker (Student Member, IEEE) received the B. Eng. and M. Eng. degrees in electronic engineering, both with distinction, from the University of Pretoria, Pretoria, South Africa, in 2017 and 2019, respectively. Since 2020, she is pursuing a doctorate (Ph.D.E.E) degree at the Institute of Radio Frequency Engineering and Electronics (IHE) at the Karlsruhe Institute of Technology, Karlsruhe, Germany. Her work focuses on antennas and packaging solutions for radar and communication applications at millimeter-wave frequencies. She received the iWAT Best Paper Award and the EuMC Best Paper Award, both in 2022.

Luca Valenziano (Student Member, IEEE) received the master's degree in electrical engineering from the University of Applied Sciences Karlsruhe (HKA), Karlsruhe, Germany, in 2022. He is currently working as a Research Associate with the Institute of Radio Frequency Engineering and Electronics (IHE), Karlsruher Institute of Technology (KIT). His main fields of research interests focus on concepts for millimeter-wave (mmW) packaging and ultra-broadband packaging of electro-optical systems.

Joel Dittmer (Student Member, IEEE) was born in Karlsruhe, Germany, in 1995. He received the B.Sc. and M.Sc. degrees in electrical engineering from the Karlsruhe Institute of Technology, Karlsruhe, Germany, in 2020 and 2022, respectively. He joined the Institute of Photonics and Quantum Electronics (IPQ) at the Karlsruhe Institute of Technology in 2023, where he started as a research assistant in the field of optoelectronic and electronic generated Terahertz signals for wireless communications. His research interests include THz system design, THz package design, and high data rate digital signal processing.

Martin Roemhild (Member, IEEE) received the B.Sc. and M.Sc. degrees in electrical engineering at the University of Stuttgart, Germany, in 2019 and 2021, respectively. In 2022, he joined the Institute for Large Area Microelectronics (IGM) at the University of Stuttgart as a scientific staff member. Since then, his main fields of research have included technological development in thin film technology and additive manufacturing to fabricate mmWave packaging.

Holger Baur is deputy manager of the laboratory for display technology of the Institute for Large Area Microelectronics at the University of Stuttgart, Germany. Holger Baur received his Dipl.-Ing. (master) Degree in Electrical Engineering from the University of Stuttgart in October 2000. Since November 2000, he is with the Institute for Large Area Microelectronics (formerly Chair of Display Technology). His main fields of research are on development of different Thin Film Transistor technologies and thin film circuitry for active matrix and advanced packaging applications.

Fabian Thome received the Dipl.-Ing. degree in electrical engineering and information technologies from the Karlsruhe Institute of Technology, Karlsruhe, Germany, in 2011 and the Ph.D. degree in the field of semiconductor devices and wireless communication from the University of Freiburg, Freiburg im Breisgau, Germany, in 2020. In 2010, he joined the Fraunhofer Institute for Applied Solid State Physics IAF, Freiburg im Breisgau, Germany, where he has been a Senior Research Scientist and a Project Manager. Since 2023, he has been the Head of the System-Oriented RF Circuits group and Deputy Head of the High Frequency Electronics Business Unit. His current research interests include the development of InGaAs and GaN HEMT technologies as well as the design and characterization of linear and nonlinear semiconductor devices and monolithic microwave integrated circuits from the microwave to submillimeter-wave frequency range for applications in radio astronomy, wireless communications, quantum computing, and measurement equipment. Dr. Thome was a recipient of the 2023 IEEE Microwave and Wireless Technology Letters Tatsou Itoh Award. In 2024, Dr. Thome received the Advanced Practice Paper Award at IMS2024.

Axel Tessmann received the Dipl.-Ing. degree in electrical engineering from the University of Karlsruhe, Germany, in 1997 and the Ph.D. degree in electrical engineering from the University of Karlsruhe, Germany, in 2006. In 1997, he joined the Microelectronics Department, Fraunhofer Institute for Applied Solid State Physics (IAF), Freiburg, Germany, where he is involved in the development of monolithically integrated circuits and subsystems for high-resolution imaging systems and high data rate wireless communication links. His main research areas are the design and packaging of millimeter-wave and submillimeter wave ICs as well as circuit simulation and linear and nonlinear device modeling. He is currently Group Manager of the millimeter wave packaging and subsystem group at the Fraunhofer IAF.

Michael Kuri received the Diploma degree in electronics from Hochschule Furtwangen University, Furtwangen im Schwarzwald, Germany, in 1996. From 1996 to 2000, he was with a PCB manufacturer, where he was involved in designing and routing high-speed/high-frequency digital and analog circuits. In 2000, he joined the High Frequency Devices and Circuits Department, Fraunhofer Institute for Applied Solid State Physics, Freiburg im Breisgau, Germany, where he is involved in the RF measurement section and with the packaging section, and designing analog and digital circuits.

Tom Neerfeld received the B.Sc. (NanoEngineering) and M.Sc. (electrical engineering) degrees from the University of Duisburg-Essen, Duisburg, Germany, in 2020 and 2023, respectively. He is currently working toward the Ph.D. degree as a Research Assistant with the department of Optoelectronics at the University of Duisburg-Essen with a focus on high speed photodiodes and system integration.

Andreas Stöhr (Senior Member, IEEE) received the Dipl.-Ing. and Dr.-Ing. degrees in electrical engineering from Gerhard-Mercator University, Duisburg, Germany, in 1991 and 1997, respectively. From 1996 to 2013, he was a Research Scientist at the University of Duisburg-Essen (UDE), Duisburg. Between 1998 and 1999, he joined the Communications Research Laboratory, Tokyo, Japan. He was with France Telecom Orange Labs, France, in 2009, and Corning, in 2015. Since 2011, he has been a Professor and the Head of the Center for Semiconductor Technology and Optoelectronics, Optoelectronics Department, UDE. He has authored or coauthored more than 200 papers in journals and conferences. His research interests include III/V integrated microwave photonics and RF photonic integration for millimeterwave and THz communications, measurement systems, and sensing applications. He is Senior Member of the IEEE Photonics and MTT Society, committee member and the chair of a number of international conferences, and the Guest Editor of IEEE/OSA.

Sebastian Randel (Senior Member, IEEE) received the Dr.-Ing. degree for his work on high-speed optical-time-division-multiplexed transmission systems from Technische Universität Berlin, Berlin, Germany, in 2005. He is currently a full Professor with the Karlsruhe Institute of Technology, Karlsruhe, Germany, where he is co-heading the Institute of Photonics and Quantum Electronics. From 2005 to 2010, he was a Research Scientist with Siemens Corporate Technology, Munich, Germany, where he led research and standardization activities in the fields of polymer-optical-fiber communications, visible-light communications, and optical access networks. From 2010 to 2016, he was a Member of Technical Staff with Bell Laboratories, Holmdel, NJ, USA. His current research focuses on high-capacity power-efficient optical and (sub-)THz communication systems and networks.

Christian Koos received the Ph.D. (Dr.-Ing.) degree in electrical engineering from the University of Karlsruhe, Karlsruhe, Germany, in 2007. He is currently a full Professor with the Karlsruhe Institute of Technology, Karlsruhe, Germany, where he is heading the Institute of Photonics and Quantum Electronics. He has co-founded several start-up companies, such as Vanguard Photonics GmbH, Vanguard Automation GmbH, SilOriX GmbH, and DeepLight SA. From 2008 to 2010, he was affiliated with the Corporate Research and Technology Department of Carl Zeiss AG in Oberkochen, Germany, where he led the technology forecast in the area of nanotechnology. He is the author of more than 140 journal papers and more than 30 patent families. His research interests include silicon photonics and hybrid integration concepts along with the associated applications in high-speed communications, optical sensing and metrology, and ultra-fast photonic-electronic signal processing. He was the recipient of several research awards and prestigious grants, such as the ERC Starting Grant in 2011 and ERC Consolidator Grant in 2017.

Norbert Fruehauf received his Ph.D. (Dr-Ing.) in Electrical Engineering from the University of Stuttgart, Germany and has more than 30 years of experience in designing and characterising liquid crystal light modulators and displays. From 1998 to 2001 he worked for Physical Optics Corporation , Torrance, California, USA, where he developed tunable micro-optic components, various display systems and integrated optical components. In 2001, he was appointed full professor heading the Chair of Display Technology (since 2011 Institute for Large Area Microelectronics) at the University of Stuttgart, Germany, where he specializes in large area microelectronics for applications in flexible displays, AMOLEDs and AMLCDs and sensor arrays. Prof. Fruehauf is the inventor of the active matrix OLED pixel circuit with external compensation used in all worldwide sold active matrix OLED TVs, which was licensed to LG Display in 2021.

Thomas Zwick (Fellow, IEEE) received his Dipl.-Ing. (M.S.E.E.) and Dr.-Ing. (Ph.D.E.E.) degrees from Universität Karlsruhe (TH), Germany, in 1994 and 1999, respectively. He was a research assistant at the Institut für Höchstfrequenztechnik und Elektronik (IHE) at Universität Karlsruhe from 1994 to 2001, then joined IBM T. J. Watson Research Center in 2001. From 2004 to 2007, he managed the RF development team for automotive radars at Siemens AG. In 2007, he became a full professor at the Karlsruhe Institute of Technology (KIT), where he directs IHE. He is author or co-author of over 400 papers and 20 patents, receiving more than 20 best paper awards. He has served on the technical program committees of various conferences, including as general chair for iWAT 2013 and IEEE MTT-S ICMIM 2015. He was TPC chair for the European Microwave Conference in 2013 and General TPC Chair for European Microwave Week in 2017. From 2008 to 2015, he was president of the Institute for Microwaves and Antennas (IMA). Recognized as a distinguished microwave lecturer from 2013 to 2015, he has been a member of the Heidelberg Academy of Sciences since 2017, an IEEE Fellow since 2018, and a member of acatech since 2019. In 2022, he received an honorary doctorate from the Budapest University of Technology and Economics.

Akanksha Bhutani (Senior Member, IEEE) obtained her M.Sc. and Ph.D. degrees in Electrical Engineering and Information Technology from the Karlsruhe Institute of Technology (KIT), Germany, in 2012 and 2019, respectively. From 2012 to 2019, she served as a Research Associate at the Institute of Radio Frequency Engineering and Electronics (IHE), KIT. Since 2021, she has been leading the Antennas and Packaging research group at IHE, KIT. Her primary research revolves around sub-THz antennas and packaging for radar and wireless communication systems. Her contributions have garnered notable recognition, including the ”Carl Freundenberg Prize” and the ”Suedwestmetall Advancement Award” for her outstanding dissertation in 2019 and 2020, respectively. Additionally, she received the IEEE Microwave Magazine Best Paper Award in 2017 and the European Microwave Week (EuMW) Best Paper Awards in 2019 and 2022. In 2023, she served as the Operations Officer at EuMW 2023, held in Berlin. Later that year, she was honored with the prestigious International IHP “Wolfgang Mehr” Fellowship Award by the Leibniz Institute for High Performance Microelectronics (IHP). She has authored and co-authored over 60 research papers published in peer-reviewed conference proceedings and scientific journals.